

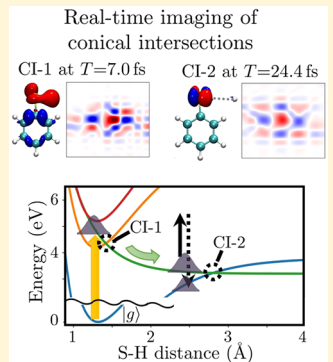
Stimulated X-ray Raman Imaging of Conical Intersections

Daeheum Cho*^{id} and Shaul Mukamel*^{id}

Department of Chemistry, University of California, Irvine, California 92697-2025, United States

Supporting Information

ABSTRACT: The conical intersection dynamics of thiophenol is studied theoretically using the stimulated X-ray Raman imaging (SXRI) technique. SXRI employs a hard X-ray narrowband/broadband hybrid probe field and provides a real-time and real-space image of the passage through conical intersections. The signal, calculated using the minimal-coupling radiation/matter Hamiltonian, carries the phase information, and the real-space image of the transition charge density can be reconstructed by its Fourier transform. The two conical intersections (S_2/S_1 ($1^1\pi\pi^*/1^1\pi\sigma^*$) and S_1/S_0 ($1^1\pi\sigma^*/S_0$)) can be distinguished and identified by the diffraction patterns in the level crossing regimes.



Nonadiabatic dynamics where the Born–Oppenheimer approximation breaks down is important in many photochemical reactions.¹ Nonadiabatic effects become strong at conical intersections (CIs), where two or more electronic surfaces become energetically degenerate and the coupling between the electronic and nuclear degrees of freedom are strong, as their time scale separation no longer holds. CIs provide effective and ultrafast nonradiative electronic decay channels for excited molecules. CIs play a key role in many chemical and biophysical processes, such as internal conversion, intersystem crossing, charge transfer, photoisomerization, and photodissociation.^{2–8} Probing and characterizing CIs has been a primary goal for understanding photochemical reactions. Several techniques for probing conical intersections^{9,10} have been proposed based on monitoring state populations,^{9,10} transient vibrational/visible spectra,^{11–14} and photoionization spectra.¹⁵ The direct unambiguous experimental observation of CIs in molecules is an open challenge. Spectroscopic techniques that probe an intrinsic property of CIs, such as electronic coherence, strong transition dipole moment, zero transition energy, are necessary.

In this paper, we propose a stimulated X-ray Raman imaging (SXRI) technique for monitoring the real-time and real-space imaging of the transition charge density at the CI. So far, stimulated X-ray diffraction has not been realized experimentally but has been predicted theoretically (sum-frequency-generation diffraction)¹⁶ and should be feasible with intense free electron laser sources. An electronic coherence is created at the CI in the course of the nonadiabatic dynamics. A hybrid X-ray probe field composed of femtosecond narrowband (probe) and attosecond broadband (stimulated emission) pulses then provides a space-resolved image of the electronic coherence at the CI thanks to the short wavelength of the X-ray probe field. The signal does carry phase information,^{16–19} and the real-space image of the transition charge density can be

reconstructed by its Fourier transform. The resulting real-time movie^{20–23} monitors the real-space image of the charge density. Conventional diffraction measurement, in contrast, provides the modulus square of the charge density and misses all phase information. This is known as the crystallographic phase problem.^{24,25} The SXRI technique provides a background-free probe for CIs. We apply the technique to probe CI dynamics in the photodissociation of the S–H bond in thiophenol after an excitation by XUV light to the S_2 ($1^1\pi\pi^*$) state (See Figure 1). Earlier studies have shown two conical intersections, CI-1 (S_2/S_1 ($1^1\pi\pi^*/1^1\pi\sigma^*$) crossing) and CI-2 (S_1/S_0 ($1^1\pi\sigma^*/S_0$) crossing) depicted in Figure 1c, serve as nonadiabatic relaxation channels.^{3,26–29} We employed the surface hopping classical trajectory method^{30,31} to simulate the conical intersection dynamics of thiophenol. The transition charge density variation across the CIs is monitored in real-time and real-space using the stimulated X-ray diffraction patterns calculated here.

THE SXRI SIGNAL

Figure 1 shows (a) the SXRI setup, (b) the corresponding diagram, and (c) the energy level scheme for the SXRI signal. A preparation process (gray box) creates a nuclear wavepacket in the $|a\rangle\langle a|$ excited state launching the nonadiabatic dynamics at time delay $T = 0$ (see Figure 1c for the notation for electronic states). Electronic coherence is created only as the wavepacket approaches the CI and is not created by the initial preparation ($\rho_{ab}(T = 0) = 0$). A hybrid probe pulse composed of a hard X-ray narrowband femtosecond pulse \mathcal{A}_0 and a hard X-ray broadband attosecond pulse \mathcal{A}_1 then generates the SXRI

Received: October 15, 2019

Accepted: November 27, 2019

Published: November 28, 2019

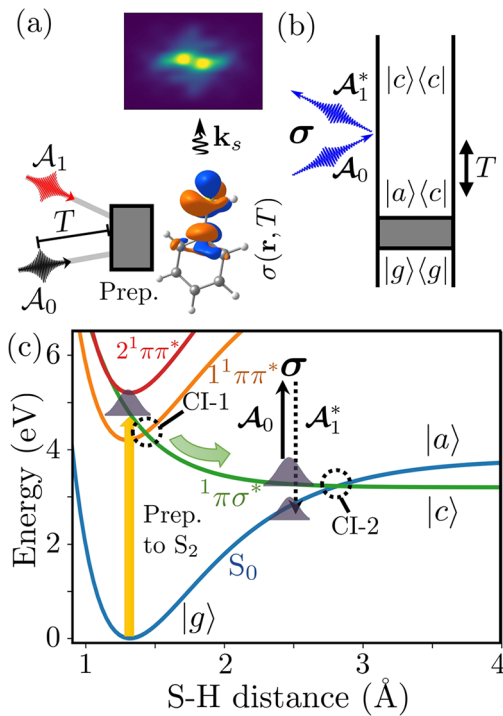


Figure 1. (a) Pulse configuration for the SXRI technique, (b) ladder diagram, and (c) energy level scheme with schematic diabatic potential energy surface along the S–H bond distance. A narrowband femtosecond X-ray pulse \mathcal{A}_0 scatters off the real-space charge density $\sigma(\mathbf{r}, t)$ of a molecule after time delay T following the arbitrary preparation (gray box) of an initial nonstationary electronic population state at $T = 0$, where \mathbf{k}_s is the wave-vector of the signal field. The signal field emission is then stimulated by a broadband attosecond X-ray pulse \mathcal{A}_1 . $|g\rangle$ denotes the ground electronic state, and $|a\rangle$ and $|c\rangle$ denote the valence electronic states including $|g\rangle$. S_i denotes an i th lowest adiabatic electronic states. $^1\pi\sigma^*$, $^1\pi\pi^*$, and $^2\pi\pi^*$ are notations for diabatic electronic states.

signal at time delay T . The narrowband pulse \mathcal{A}_0 scatters off the electronic transition charge density $\sigma_{ij}(\mathbf{r}, t)$ (see eqs 1 and 4) and the broadband pulse \mathcal{A}_1 stimulates the Raman emission. The diffracted signal (see eq 10) is recorded by varying the angle between the two probe fields to generate the wavevector-resolved diffraction pattern, i.e., Q -resolution in Figure 4, where $Q = \mathbf{k}_0 - \mathbf{k}_1$ is the momentum transfer and \mathbf{k}_i is the wave-vector of the field \mathcal{A}_i . Frequency-dispersion of the broadband pulse \mathcal{A}_1 reveals the Raman resonances. Using the narrowband frequency ω_0 as a reference, an emitted signal field at positive (negative) detection frequency represents a Stokes (anti-Stokes) process.

The SXRI signal was calculated using the minimal-coupling Hamiltonian for the radiation–matter interaction which in the off-resonant regime reads³²

$$\hat{H}_{\text{int}} = \frac{1}{2} \int d\mathbf{r} \hat{\sigma}(\mathbf{r}) \hat{\mathbf{A}}_1(\mathbf{r}, t) \cdot \hat{\mathbf{A}}_0(\mathbf{r}, t) \quad (1)$$

(in atomic units) where $\hat{\sigma}(\mathbf{r})$ is the charge density operator and $\hat{\mathbf{A}}_0(\mathbf{r}, t)$ and $\hat{\mathbf{A}}_1(\mathbf{r}, t)$ are the femtosecond (narrowband) and attosecond (broadband) vector potentials, respectively. The charge density operator is given by

$$\hat{\sigma}(\mathbf{r}) = \hat{\psi}^\dagger(\mathbf{r}) \hat{\psi}(\mathbf{r}) \quad (2)$$

where $\hat{\psi}^\dagger(\mathbf{r})$ is the electron field annihilation (creation) operator, which satisfies the Fermi anticommutation relation $\{\hat{\psi}(\mathbf{r}), \hat{\psi}^\dagger(\mathbf{r}')\} = \delta(\mathbf{r} - \mathbf{r}')$. The vector potential is expanded in field modes

$$\hat{\mathbf{A}}(\mathbf{r}) = \sum_{\mathbf{k}, \lambda} \sqrt{\frac{2\pi}{\Omega \omega_j}} (\epsilon^{(\lambda_j)}(\mathbf{k}_j) \hat{a}_j e^{i\mathbf{k}_j \cdot \mathbf{r}} + \epsilon^{(\lambda_j)*}(\mathbf{k}_j) \hat{a}_j^\dagger e^{-i\mathbf{k}_j \cdot \mathbf{r}}) \quad (3)$$

where \hat{a}_j^\dagger is the photon field boson annihilation (creation) operator for mode j , Ω the field quantization volume, \mathbf{k}_j the wave-vector, and $\epsilon^{(\lambda_j)}(\mathbf{k}_j)$ the polarization vector. The matrix element of charge-density operator $\sigma_{ij}(\mathbf{r})$ for an N -electron system is given by

$$\langle \hat{\sigma}_{ij}(\mathbf{r}, t) \rangle = N \int d\mathbf{r}_2 \dots d\mathbf{r}_N \Psi_i(\mathbf{r}, \mathbf{r}_2, \dots, \mathbf{r}_N) \Psi_j^*(\mathbf{r}, \mathbf{r}_2, \dots, \mathbf{r}_N) \quad (4)$$

where $\Psi_{i(j)}(\mathbf{r}, \mathbf{r}_2, \dots, \mathbf{r}_N)$ is the many-electron wave function of electronic eigenstate $i(j)$, with $\mathbf{r}, \mathbf{r}_2, \dots, \mathbf{r}_N$ the electronic coordinates. The transition charge density $\sigma_{ij}(\mathbf{r})$, when $i \neq j$, describes the electronic overlap between the two electronic states Ψ_i and Ψ_j . The expectation value of the charge density operator can be expressed as

$$\langle \hat{\sigma}(\mathbf{r}, t) \rangle = \sum_{i,j} \rho_{ij}(t) \sigma_{ji}(\mathbf{r}, t) \quad (5)$$

where $\rho_{ij}(t)$ are the many-electron density matrix elements in the adiabatic basis. Diffraction signal is related to the spatial Fourier transform of $\langle \hat{\sigma}(\mathbf{r}, t) \rangle$ given by

$$\langle \hat{\sigma}(\mathbf{Q}, t) \rangle = \int d\mathbf{r} e^{-i\mathbf{Q} \cdot \mathbf{r}} \langle \hat{\sigma}(\mathbf{r}, t) \rangle = \sum_{i,j} \rho_{ij}(t) \sigma_{ji}(\mathbf{Q}, t) \quad (6)$$

where $\mathbf{Q} = \mathbf{k}_1 - \mathbf{k}_0$ is the scattering momentum wavevector and

$$\sigma_{ij}(\mathbf{Q}, t) = \int d\mathbf{r} e^{-i\mathbf{Q} \cdot \mathbf{r}} \sigma_{ij}(\mathbf{r}, t) \quad (7)$$

The SXRI signal is defined as the time-integrated rate of frequency-dispersed photon number change of the attosecond (broadband) field \mathcal{A}_1

$$S(\omega, \mathbf{k}_s) = \int dt \left\langle \frac{d}{dt} \hat{N}_\omega^1 \right\rangle \quad (8)$$

where \hat{N}_ω^1 is the number operator for a photon mode of the broadband pulse \mathcal{A}_1 with frequency ω and \mathbf{k}_s is the wave-vector of the signal field. Using the interaction picture equation of motion for the photon number operator \hat{N}_ω^1 with the minimal-coupling interaction Hamiltonian \hat{H}_{int} the frequency-dispersed signal finally reads

$$S(\omega, \mathbf{Q}, T) = \mathcal{J} \int dt e^{i\omega(t-T)} \mathcal{A}_1^*(\omega) \mathcal{A}_0(t-T) \langle \hat{\sigma}(\mathbf{Q}, t) \rangle \quad (9)$$

where we used $\mathcal{A}_1^*(t-T) = \int dt e^{i\omega(t-T)} \mathcal{A}_1^*(\omega)$ and assumed plane wave probe fields ($\mathcal{A}_i(\mathbf{r}, t) = \mathcal{A}_i(t) e^{i(\mathbf{k}_i \cdot \mathbf{r} + \phi_i)}$), and \mathcal{J} denotes the imaginary part (see Supporting Information for the detailed derivation).

Plugging eq 6 into eq 9, we obtain

$$\begin{aligned}
 S(\omega, \mathbf{Q}, T) &= \int dt e^{i\omega(t-T)} \mathcal{A}_1^*(\omega) \mathcal{A}_0(t-T) \\
 &\quad \times \sum_{a,c} \rho_{ac}(t) \sigma_{ac}(\mathbf{Q}, t) \\
 &= \int dt e^{i\omega(t-T)} |\mathcal{A}_1(\omega)| |\mathcal{A}_0(t-T)| \sum_{a,c} |\rho_{ac}(t)| \\
 &\quad \times \sigma_{ac}(\mathbf{Q}, t) e^{i(\phi_0 - \phi_1 + \phi_{ac}(t))} \quad (10)
 \end{aligned}$$

where $\rho_{ac}(t) = |\rho_{ac}(t)| e^{i\phi_{ac}(t)}$ is the matrix element of the many-body electronic density matrix in adiabatic basis, and $\phi_{ac}(t)$ is a time-dependent phase of the density matrix element, $\mathcal{A}_1(\omega) = |\mathcal{A}_1(\omega)| e^{i\phi_1}$, and $\mathcal{A}_0(t) = |\mathcal{A}_0(t)| e^{i\phi_0}$ where ϕ_i is the phase of the \mathcal{A}_i field. The charge density $\langle \hat{\sigma}(\mathbf{r}, t) \rangle$ can be retrieved by inverse Fourier transform of $\langle \hat{\sigma}(\mathbf{Q}, t) \rangle$, which can be obtained by deconvolution of the three-dimensional SXRI signal. The time-dependence of $\sigma_{ij}(\mathbf{r}, t)$ and $\sigma_{ij}(\mathbf{Q}, t)$ arises from the nuclear dynamics. The signals presented in Figures 4 and S1 are calculated using eq 10 for $\phi_0 - \phi_1 = 0$. Because the signal is linear in the probe field amplitudes $\mathcal{A}_1 \mathcal{A}_0$, it carries the phase factor $e^{i(\phi_0 - \phi_1)}$. Controlled phases ($\phi_0 - \phi_1$) are required to generate a finite SXRI signal; the signal vanishes upon averaging over a random phase probe pulse. Note that when the two probe field phases are the same, $\phi_0 = \phi_1$, the phase of the electronic coherence $\phi_{ac}(t)$ can be directly measured by the signal. The signal from populations (diagonal elements, ρ_{aa}) vanishes because it has no dynamical phase $\phi_{aa}(t) = 0$. The SXRI signal therefore provides a background-free image of the electronic coherences ρ_{ac} created in the vicinity of the CI. Frequency-resolved stimulated Raman resonance between the wavepacket on two surfaces may allow detection of the time-resolved energy splitting and the potential energy surface gradient in coordinate space.

SXRI is an extension of the TRUECARS (transient redistribution of ultrafast electronic coherences in attosecond Raman signals) technique,³³ which can probe the conical intersection in real-time with a stimulated Raman probe. The difference is that by using hard X-rays, we obtain an image of the transition charge density. This requires working with the minimal-coupling Hamiltonian for the radiation–matter interaction.

SURFACE HOPPING NONADIABATIC DYNAMICS OF THIOPHENOL

Modeling the strongly coupled electronic and nuclear degrees of freedom in photochemical reactions is a computational challenge. Simulation protocols that go beyond the Born–Oppenheimer approximation include (multiconfigurational) Ehrenfest dynamics,³⁴ multiconfigurational time dependent Hartree,³⁵ multiple spawning,³⁶ and semiclassical approaches, which treat the electrons quantum mechanically and the nuclear degrees of freedom classically and provide a practical level of theory to describe nonadiabatic dynamics in polyatomic molecules. Surface hopping^{30,31} is the most commonly used semiclassical nonadiabatic dynamics protocol. Because the trajectories do not communicate with each other, a careful treatment needs to be made for the description of the nuclear coherences.

The surface hopping simulation protocol implemented in the SHARC^{37,38} program was employed to simulate the nonadiabatic photodissociation of thiophenol. Details of the

protocol are given in ref 38. Herein, we provide a brief summary (see Supporting Information for computational details). The electronic structure calculations were performed using the MOLPRO³⁹ program at the state-averaged CASSCF-(4/6)/6-31G* level of theory with the four lowest adiabatic electronic states taken into account. The local diabatization algorithm based on the overlap matrices between the adiabatic electronic states $\langle \psi_\beta(t) | \psi_\alpha(t + \Delta t) \rangle$ is used to propagate the electronic wave function under the effect of nonadiabatic couplings. We employed the energy-based decoherence correction scheme to describe the electronic decoherence when two surfaces drift away after passing the CI.⁴⁰ The electronic population (ρ_{ii} ; diagonal element of the density matrix) and the coherence (ρ_{ij} ; off-diagonal element of the density matrix) in the adiabatic electronic state can be calculated from the wave function coefficient vector $c(t)$, $\rho_{ii}(t) = |c_i(t)|^2$ and $\rho_{ij}(t) = c_i(t)c_j^*(t)$. The Raman shift $|\Delta E_{ij}|$ was obtained from the energy difference between the adiabatic electronic states S_i and S_j . The transition charge density $\sigma_{ij}(\mathbf{r})$ is calculated at every nuclear time step to account the geometrical change. All quantities presented in the paper are in the adiabatic electronic basis. The total propagation time was 49 fs, and the time steps for propagation of the nuclear and the electronic degrees of freedom were 0.05 and 0.002 fs, respectively. Forty-five initial geometries were sampled by using the quantum harmonic oscillator Wigner distribution at around the ground state equilibrium geometry. The non-adiabatic surface hopping dynamics was initiated by promoting the system on S_2 ($^1\pi\sigma^*$) state. Forty-five trajectories were simulated and averaged out to provide the signals. Figures S2–4 shows the convergence of the population dynamics ρ_{ii} and coherences ρ_{12} and ρ_{01} with the number of trajectories taken into account.

We investigated the dynamics of the S–H dissociation of thiophenol that takes place after its initial photoexcitation in the S_2 ($^1\pi\sigma^*$) state (impulsive excitation approximation; no external pump pulse was taken into account in the surface hopping dynamics). In practice, excitation at long wavelength $\lambda > 275$ nm excites the system to the $1^1\pi\pi^*$ state, while the $^1\pi\sigma^*$ state can be excited at shorter excitation wavelengths.^{26,27,41} H-tunnelling from the $1^1\pi\pi^*$ state to the $^1\pi\sigma^*$ state may play a role in the photodissociation of thiophenol after an excitation to the S_1 ($1^1\pi\pi^*$) state, which may not be properly described by the semiclassical surface hopping method. It is known that H-tunnelling plays an important role in a photodissociation of phenol after excitation to the S_1 ($1^1\pi\pi^*$) state.^{42–44} Therefore, a photodissociation dynamics following an initial excitation to the S_2 ($^1\pi\sigma^*$) state was considered in this paper.

Figure 2 shows the populations ρ_{ii} , absolute value of coherences $|\rho_{ij}|$, Raman shifts $|\Delta E_{ij}|$, and the probability distribution of R_{S-H} vs time delay T . The initially excited S_2 population at $T = 0$ relaxes to the ground state S_0 through the two conical intersections. As the excited system at the S_2 surface approaches the S_2/S_1 CI (CI-1), electronic coherence between S_2 and S_1 ($|\rho_{12}|$) builds up and peaks at 7 fs. At the same time, the S_2 population transfers to S_1 during $T = 3–13$ fs, i.e. ρ_{22} sharply decreases and ρ_{11} increases. A sharp drop of the energy gap between S_2 and S_1 ($|\Delta E_{12}|$) from 1.3 eV at $T = 0$ fs to 0 at $T = 3–8$ fs occurs, and the two electronic surfaces become degenerate. As the excited system through CI-1, $|\rho_{12}|$ decreases, and $|\Delta E_{12}|$ increases. Up to $T = 13$ fs, the S–H bond length R_{S-H} does not significantly vary as there is no major

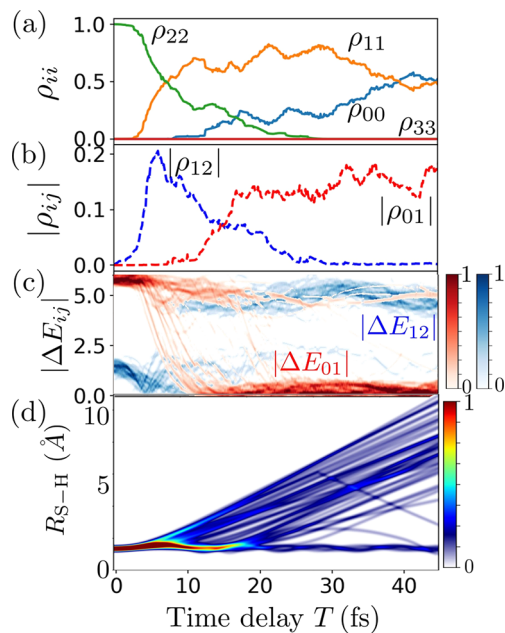


Figure 2. (a) Population ρ_{ij} , (b) absolute value of electronic coherence $|\rho_{ij}|$, (c) the probability distribution of Raman shift $|\Delta E_{ij}|$ (color code; blue for $|\Delta E_{12}|$ and red for $|\Delta E_{01}|$), and (d) the probability distribution of R_{S-H} vs the time delay T .

change between the ground and the CI-1 geometries, merely a 0.2 Å change in S-H distance (as shown in Figure 2a).

The nonadiabatic dynamics between CI-1 to CI-2 involves a significant geometrical change associated with the S-H bond breaking. As the excited system approaches CI-2 at $T = 13$ fs, the electronic coherence $|\rho_{01}|$ and thus the ground state population ρ_{00} start to grow. The energy gap $|\Delta E_{01}|$ then sharply drops from 6 eV to 0.

For better visualization of the distribution of the S-H distance in the course of the nonadiabatic dynamics, Figure 3 shows slices of Figure 2d and an overlay of corresponding geometries of 45 trajectories at selected time delays T . There is no significant geometrical rearrangement up to 5 fs. A noticeable S-H bond stretching starts at $T = 10$ fs. The nonadiabatic dynamics from CI-1 to CI-2 accompanies a significant deviation of the S-H bond distance from equilibrium.

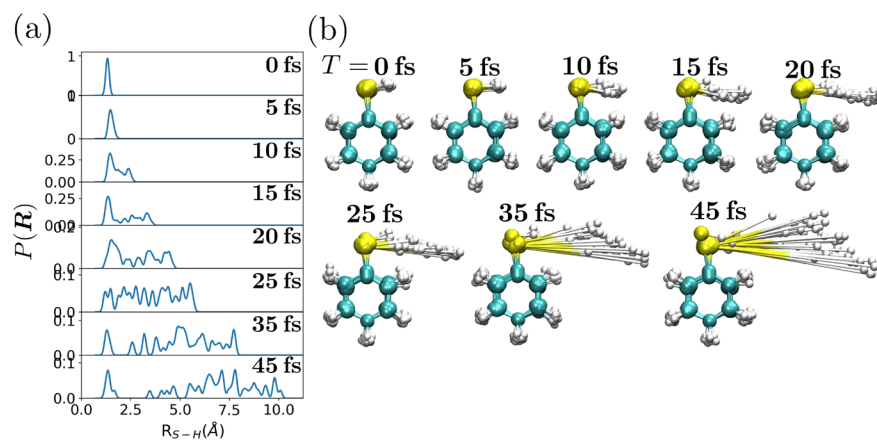


Figure 3. (a) Time-dependent probability map of the S-H bond distance R_{S-H} for various delays as indicated. (b) Overlay of geometries from all trajectories at various time delays T .

After passing CI-2, the molecule may experience the S-H bond breaking (Figure 2d). Long-lived electronic coherence $|\rho_{01}|$ indicates that passing through CI-2 takes longer than CI-1. Some of the trajectories did not completely pass CI-2 in the 49 fs observation window of our simulation.

■ SIGNATURES OF CONICAL INTERSECTIONS IN THE SXRI SIGNAL

Figure 4 shows the simulated SXRI signal for the nonadiabatic dynamics of thiophenol at several time delays T . The total signal $S_{\text{total}} = \sum_{ij} S_{ij}$ and two dominant contributions S_{12} and S_{01} are shown to highlight the signal contributions at CI-1 and CI-2, where S_{ij} is the signal contributed by $|i\rangle\langle j|$ coherence. S_{12} (S_{01}) is a signature of $|1\rangle\langle 2|$ ($|0\rangle\langle 1|$) coherence at the CI-1 (CI-2). The top, middle, and bottom panels show S_{12} , S_{01} , and S_{total} , respectively. As shown in Figure 4, S_{12} turns on at $T = 7$ fs where the excited system reaches the CI-1, as evidenced by a large electronic coherence $|\rho_{12}|$ and small Raman shift $|\Delta E_{12}|$. As the excited system passed through CI-1 at $T = 7$ fs, S_{12} fades away. S_{01} is turned on at $T = 12.8$ fs as the system reaches CI-2 where the ground and the first excited states cross. This is revealed by the fact that electronic coherence $|\rho_{01}|$ starts to grow, and the Raman shift $|\Delta E_{01}|$ becomes negligibly small at $T = 12.8$ fs. Therefore, the SXRI signal is a manifestation of the conical intersection.

Figure 5 depicts the product of off-diagonal density matrix element and the corresponding transition charge density $|\rho_{ij}(T)|\sigma_{ji}(\mathbf{r},T)$ created by $|i\rangle\langle j|$ coherence, which is responsible for the SXRI signal S_{ij} shown in Figure 4. The $|\rho_{12}(t)|\sigma_{12}(\mathbf{r},t)$ associated with CI-1 accounts for the electron transfer between a phenol and a S-H moiety while the $|\rho_{01}(t)|\sigma_{01}(\mathbf{r},t)$ associated with CI-2 accounts for mostly on site electron rearrangement at the sulfur atom. Clear distinction between the $|\rho_{ij}(t)|\sigma_{ji}(\mathbf{r},t)$ associated with conical intersections is revealed by the SXRI pattern. Figure 5 is created by using the real space transition charge density $\sigma_{ij}(\mathbf{r},T)$ and the density matrix element $\rho_{ij}(T)$, and $\langle \hat{\sigma}(\mathbf{r},T) \rangle$ can be reconstructed by three-dimensional inverse Fourier transform of $\langle \hat{\sigma}(\mathbf{r},T) \rangle$ obtained by deconvolution of the SXRI signal.

■ CONCLUSIONS

We proposed a stimulated X-ray Raman imaging technique for probing nonadiabatic molecular dynamics. The technique

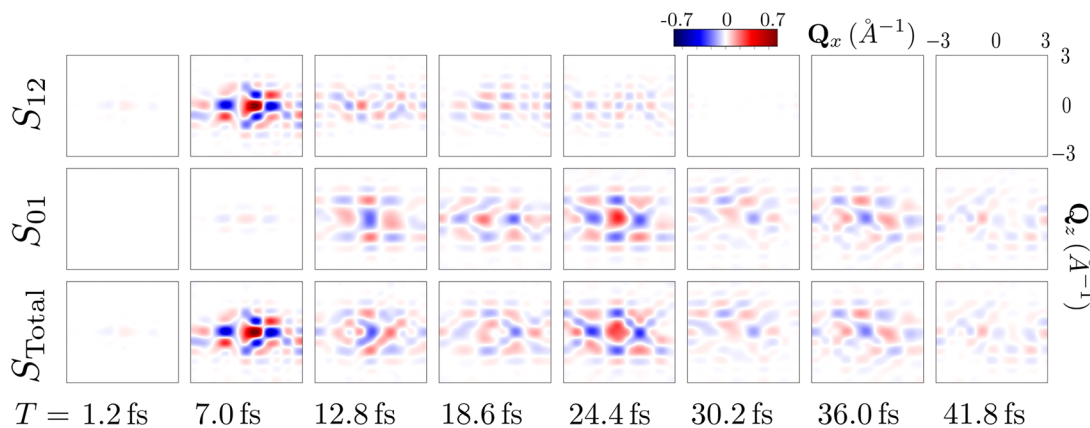


Figure 4. Simulated SXRI signal $S(\omega, Q, T)$ (eq 10) for $\omega = 0.5$ eV for several time delays T . The total signal $S_{\text{total}} = \sum_{ij} S_{ij}$ and two dominant contributions S_{12} and S_{01} are shown to highlight the signal contributions at CI-1 and CI-2, where S_{ij} is the signal contributed by $|i\rangle\langle j|$ coherence. S_{12} (S_{01}) is a signature of $|1\rangle\langle 2|$ ($|0\rangle\langle 1|$) coherence at the CI-1 (CI-2). A two-dimensional slice of Q_x - Q_z plane at $Q_y = 0 \text{ \AA}^{-1}$ is given. $\langle \sigma(Q, t) \rangle$ can be obtained by deconvolution of the three-dimensional SXRI signal (see Supporting Information Figure S1 for the same signals for $\omega = 1.5$ and -0.5 eV).

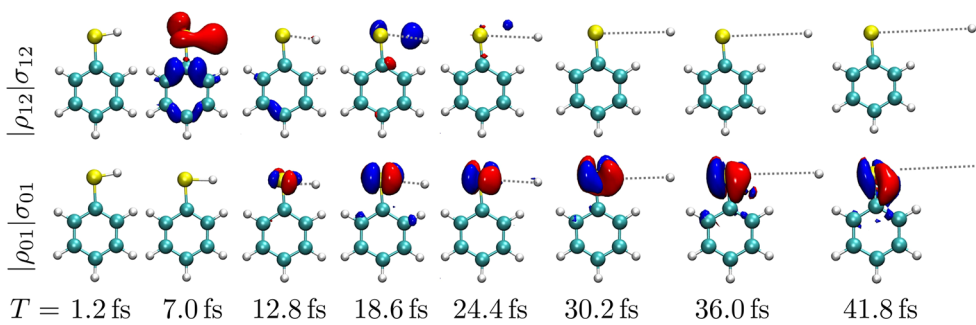


Figure 5. Isosurface plot of $|\rho_{ij}(T)|\sigma_{ji}(\mathbf{r}, T)$ created by $|i\rangle\langle j|$ coherence, which is responsible for (top) S_{12} and (bottom) S_{01} signal contributions, respectively, at several time delays T . It is calculated in the real-space by using the real-space transition charge density $\sigma_{ji}(\mathbf{r}, T)$ and the density matrix element $\rho_{ij}(T)$, not by the inverse Fourier transform of the $|\rho_{ij}(T)|\sigma_{ji}(Q, T)$ obtained from the SXRI signal. Isovalue of 0.015 in atomic units was used; red: positive and blue: negative value.

employs hard X-ray narrowband/broadband hybrid probe fields to generate a space-resolved image of a transition charge density which depends on the Raman frequency and the time delay T . SXRI provides information on the electronic transition at the level crossing region. Being a stimulated diffraction technique, the signal carries phase information, and the real-space image of the transition charge density can be reconstructed by its Fourier transform. More importantly, conical intersections can be distinguished by the diffraction patterns. Computationally, the simulation of SXRI signal requires use of the minimal-coupling Hamiltonian. This provides an intuitive picture and direct characterization on the electronic transition at the CI.

ASSOCIATED CONTENT

Supporting Information

The Supporting Information is available free of charge at <https://pubs.acs.org/doi/10.1021/acs.jpclett.9b03020>.

- (1) Additional computational details; (2) derivation of the SXRI signal; (3) frequency-resolved SXRI signal; (4) convergence of the population dynamics ρ_{ii} , the absolute, real, and imaginary value of two dominant coherences, ρ_{01} and ρ_{12} according to number of trajectories accounted (PDF)

AUTHOR INFORMATION

Corresponding Authors

*E-mail: daeheumc@uci.edu.
*E-mail: smukamel@uci.edu.

ORCID

Daeheum Cho: [0000-0002-0322-4291](https://orcid.org/0000-0002-0322-4291)
Shaul Mukamel: [0000-0002-6015-3135](https://orcid.org/0000-0002-6015-3135)

Notes

The authors declare no competing financial interest.

ACKNOWLEDGMENTS

The support of the Chemical Sciences, Geosciences, and Biosciences division, Office of Basic Energy Sciences, Office of Science, U.S. Department of Energy through Award DE-FG02-04ER15571 and of the National Science Foundation (Grant CHE-1663822) is gratefully acknowledged. D.C. was supported by the DOE grant. This work was also supported by the National Supercomputing Center with supercomputing resources including technical support KSC-2017-S1-0004.

REFERENCES

- (1) Domcke, W.; Yarkony, D. R. Role of Conical Intersections in Molecular Spectroscopy and Photoinduced Chemical Dynamics. *Annu. Rev. Phys. Chem.* **2012**, 63, 325–352.

(2) Lim, J. S.; Kim, S. K. Experimental probing of conical intersection dynamics in the photodissociation of thioanisole. *Nat. Chem.* **2010**, *2*, 627–632.

(3) You, H. S.; Han, S.; Lim, J. S.; Kim, S. K. ($\pi\pi^*/\pi\sigma^*$) Conical Intersection Seam Experimentally Observed in the SD Bond Dissociation Reaction of Thiophenol-*d*₁. *J. Phys. Chem. Lett.* **2015**, *6*, 3202–3208.

(4) Musser, A. J.; Liebel, M.; Schnedermann, C.; Wende, T.; Kehoe, T. B.; Rao, A.; Kukura, P. Evidence for conical intersection dynamics mediating ultrafast singlet exciton fission. *Nat. Phys.* **2015**, *11*, 352–357.

(5) Worner, H. J.; Bertrand, J. B.; Fabre, B.; Higuet, J.; Ruf, H.; Dubrouil, A.; Patchkovskii, S.; Spanner, M.; Mairesse, Y.; Blanchet, V.; et al. Conical Intersection Dynamics in NO₂ Probed by Homodyne High-Harmonic Spectroscopy. *Science* **2011**, *334*, 208–212.

(6) Horio, T.; Fuji, T.; Suzuki, Y.-I.; Suzuki, T. Probing Ultrafast Internal Conversion through Conical Intersection via Time-Energy Map of Photoelectron Angular Anisotropy. *J. Am. Chem. Soc.* **2009**, *131*, 10392–10393.

(7) Hoffman, D. P.; Ellis, S. R.; Mathies, R. A. Characterization of a Conical Intersection in a Charge-Transfer Dimer with Two-Dimensional Time-Resolved Stimulated Raman Spectroscopy. *J. Phys. Chem. A* **2014**, *118*, 4955–4965.

(8) Hoffman, D. P.; Mathies, R. A. Femtosecond Stimulated Raman Exposes the Role of Vibrational Coherence in Condensed-Phase Photoreactivity. *Acc. Chem. Res.* **2016**, *49*, 616–625.

(9) Polli, D.; Alto, P.; Weingart, O.; Spillane, K. M.; Manzoni, C.; Brida, D.; Tomasello, G.; Orlandi, G.; Kukura, P.; Mathies, R. A.; et al. Conical intersection dynamics of the primary photoisomerization event in vision. *Nature* **2010**, *467*, 440–443.

(10) McFarland, B. K.; Farrell, J. P.; Miyabe, S.; Tarantelli, F.; Aguilar, A.; Berrah, N.; Bostedt, C.; Bozek, J. D.; Bucksbaum, P. H.; Castagna, J. C.; et al. Ultrafast X-ray Auger probing of photoexcited molecular dynamics. *Nat. Commun.* **2014**, *5*, 4235.

(11) Raab, A.; Worth, G. A.; Meyer, H.-D.; Cederbaum, L. S. Molecular dynamics of pyrazine after excitation to the S2 electronic state using a realistic 24-mode model Hamiltonian. *J. Chem. Phys.* **1999**, *110*, 936–946.

(12) Oliver, T. A. A.; Lewis, N. H. C.; Fleming, G. R. Correlating the motion of electrons and nuclei with two-dimensional electronic-vibrational spectroscopy. *Proc. Natl. Acad. Sci. U. S. A.* **2014**, *111*, 10061–10066.

(13) Timmers, H.; Li, Z.; Shivaram, N.; Santra, R.; Vendrell, O.; Sandhu, A. Coherent Electron Hole Dynamics Near a Conical Intersection. *Phys. Rev. Lett.* **2014**, *113*, 113003.

(14) Kowalewski, M.; Mukamel, S. Stimulated Raman signals at conical intersections: Ab initio surface hopping simulation protocol with direct propagation of the nuclear wave function. *J. Chem. Phys.* **2015**, *143*, 044117.

(15) von Conta, A.; Tehlar, A.; Schletter, A.; Arasaki, Y.; Takatsuka, K.; Worner, H. J. Conical-intersection dynamics and ground-state chemistry probed by extreme-ultraviolet time-resolved photoelectron spectroscopy. *Nat. Commun.* **2018**, *9*, 3162.

(16) Rouxel, J. R.; Kowalewski, M.; Bennett, K.; Mukamel, S. X-Ray Sum Frequency Diffraction for Direct Imaging of Ultrafast Electron Dynamics. *Phys. Rev. Lett.* **2018**, *120*, 243902.

(17) Martin, A. V.; D’Alfonso, A. J.; Wang, F.; Bean, R.; Capotondi, F.; Kirian, R. A.; Pedersoli, E.; Raimondi, L.; Stellato, F.; Yoon, C. H.; et al. X-ray holography with a customizable reference. *Nat. Commun.* **2014**, *5*, 4661.

(18) Tegze, M.; Faigel, G. X-ray holography with atomic resolution. *Nature* **1996**, *380*, 49.

(19) Marchesini, S.; Boutet, S.; Sakdinawat, A. E.; Bogan, M. J.; Bajt, S.; Barty, A.; Chapman, H. N.; Frank, M.; Hau-Riege, S. P.; Szke, A.; et al. Massively parallel X-ray holography. *Nat. Photonics* **2008**, *2*, 560–563.

(20) Zamponi, F.; Rothhardt, P.; Stingl, J.; Woerner, M.; Elsaesser, T. Ultrafast large-amplitude relocation of electronic charge in ionic crystals. *Proc. Natl. Acad. Sci. U. S. A.* **2012**, *109*, 5207–5212.

(21) Dixit, G.; Vendrell, O.; Santra, R. Imaging electronic quantum motion with light. *Proc. Natl. Acad. Sci. U. S. A.* **2012**, *109*, 5.

(22) Woerner, M.; Zamponi, F.; Ansari, Z.; Dreyer, J.; Freyer, B.; Premont-Schwarz, M.; Elsaesser, T. Concerted electron and proton transfer in ionic crystals mapped by femtosecond x-ray powder diffraction. *J. Chem. Phys.* **2010**, *133*, 064509.

(23) Hauf, C.; Hernandez Salvador, A.-A.; Holtz, M.; Woerner, M.; Elsaesser, T. Phonon driven charge dynamics in polycrystalline acetylsalicylic acid mapped by ultrafast x-ray diffraction. *Struct. Dyn.* **2019**, *6*, 014503.

(24) Harrison, R. W. Phase problem in crystallography. *J. Opt. Soc. Am. A* **1993**, *10*, 1046.

(25) Taylor, G. The phase problem. *Acta Crystallogr., Sect. D: Biol. Crystallogr.* **2003**, *59*, 1881.

(26) Devine, A. L.; Nix, M. G. D.; Dixon, R. N.; Ashfold, M. N. R. Near-Ultraviolet Photodissociation of Thiophenol. *J. Phys. Chem. A* **2008**, *112*, 9563–9574.

(27) Lim, J. S.; Choi, H.; Lim, I. S.; Park, S. B.; Lee, Y. S.; Kim, S. K. Photodissociation Dynamics of Thiophenol- *d*₁: The Nature of Excited Electronic States along the SD Bond Dissociation Coordinate. *J. Phys. Chem. A* **2009**, *113*, 10410–10416.

(28) Lim, I. S.; Lim, J. S.; Lee, Y. S.; Kim, S. K. Experimental and theoretical study of the photodissociation reaction of thiophenol at 243nm: Intramolecular orbital alignment of the phenylthiyl radical. *J. Chem. Phys.* **2007**, *126*, 11.

(29) Ashfold, M. N. R.; Devine, A. L.; Dixon, R. N.; King, G. A.; Nix, M. G. D.; Oliver, T. A. A. Exploring nuclear motion through conical intersections in the UV photodissociation of phenols and thiophenol. *Proc. Natl. Acad. Sci. U. S. A.* **2008**, *105*, 12701–12706.

(30) Tully, J. C.; Preston, R. K. Trajectory Surface Hopping Approach to Nonadiabatic Molecular Collisions: The Reaction of H⁺ with D₂. *J. Chem. Phys.* **1971**, *55*, 562–572.

(31) Subotnik, J. E.; Jain, A.; Landry, B.; Petit, A.; Ouyang, W.; Bellonzi, N. Understanding the Surface Hopping View of Electronic Transitions and Decoherence. *Annu. Rev. Phys. Chem.* **2016**, *67*, 387–417.

(32) Chernyak, V. Y.; Saurabh, P.; Mukamel, S. Non-linear non-local molecular electrodynamics with nano-optical fields. *J. Chem. Phys.* **2015**, *143*, 164107.

(33) Kowalewski, M.; Bennett, K.; Dorfman, K. E.; Mukamel, S. Catching Conical Intersections in the Act: Monitoring Transient Electronic Coherences by Attosecond Stimulated X-Ray Raman Signals. *Phys. Rev. Lett.* **2015**, *115*, 193003.

(34) Shalashilin, D. V. Multiconfigurational Ehrenfest approach to quantum coherent dynamics in large molecular systems. *Faraday Discuss.* **2011**, *153*, 105.

(35) Meyer, H.-D.; Worth, G. A. Quantum molecular dynamics: propagating wavepackets and density operators using the multi-configuration time-dependent Hartree method. *Theor. Chem. Acc.* **2003**, *109*, 251–267.

(36) Ben-Nun, M.; Quenneville, J.; Martinez, T. J. Ab Initio Multiple Spawning: Photochemistry from First Principles Quantum Molecular Dynamics. *J. Phys. Chem. A* **2000**, *104*, 5161–5175.

(37) Mai, S.; Marquetand, P.; Gonzalez, L. Nonadiabatic dynamics: The SHARC approach. *WIREs Comput. Mol. Sci.* **2018**, *8*, No. e1370.

(38) Richter, M.; Marquetand, P.; Gonzalez-Vazquez, J.; Sola, I.; Gonzalez, L. SHARC: ab initio Molecular Dynamics with Surface Hopping in the Adiabatic Representation Including Arbitrary Couplings. *J. Chem. Theory Comput.* **2011**, *7*, 1253–1258.

(39) Werner, H.-J.; Knowles, P. J.; Knizia, G.; Manby, F. R.; Schutz, M. Molpro: a general-purpose quantum chemistry program package. *WIREs Comput. Mol. Sci.* **2012**, *2*, 242–253.

(40) Granucci, G.; Persico, M.; Zocante, A. Including quantum decoherence in surface hopping. *J. Chem. Phys.* **2010**, *133*, 134111.

(41) Venkatesan, T. S.; Ramesh, S. G.; Lan, Z.; Domcke, W. Theoretical analysis of photoinduced H-atom elimination in thiophenol. *J. Chem. Phys.* **2012**, *136*, 174312.

(42) Yang, K. R.; Xu, X.; Zheng, J.; Truhlar, D. G. Full-dimensional potentials and state couplings and multidimensional tunneling

calculations for the photodissociation of phenol. *Chem. Sci.* **2014**, *5*, 4661–4680.

(43) Xu, X.; Zheng, J.; Yang, K. R.; Truhlar, D. G. Photodissociation Dynamics of Phenol: Multistate Trajectory Simulations including Tunneling. *J. Am. Chem. Soc.* **2014**, *136*, 16378–16386.

(44) Xie, C.; Ma, J.; Zhu, X.; Yarkony, D. R.; Xie, D.; Guo, H. Nonadiabatic Tunneling in Photodissociation of Phenol. *J. Am. Chem. Soc.* **2016**, *138*, 7828–7831.